JOURNAL OF AGRICULTURAL AND FOOD CHEMISTRY

Article

pubs.acs.org/JAFC

Computational Study Exploring the Interaction Mechanism of Benzimidazole Derivatives as Potent Cattle Bovine Viral Diarrhea Virus Inhibitors

Jinghui Wang,[†,‡,§] Yinfeng Yang,[†,‡,§] Yan Li,[†,‡] and Yonghua Wang*[,†]

[†]Key Laboratory of Xinjiang Endemic Phytomedicine Resources, Pharmacy School, Ministry of Education, Shihezi University, Shihezi 832002, China

[‡]Key Laboratory of Industrial Ecology and Environmental Engineering (MOE), Faculty of Chemical, Environmental and Biological Science and Technology, Dalian University of Technology, Dalian, Liaoning 116024, P. R. China

Supporting Information

ABSTRACT: Bovine viral diarrhea virus (BVDV) infections are prevailing in cattle populations on a worldwide scale. The BVDV RNA-dependent RNA polymerase (RdRp), as a promising target for new anti-BVDV drug development, has attracted increasing attention. To explore the interaction mechanism of 65 benzimidazole scaffold-based derivatives as BVDV inhibitors, presently, a computational study was performed based on a combination of 3D-QSAR, molecular docking, and molecular dynamics (MD) simulations. The resultant optimum CoMFA and CoMSIA models present proper reliabilities and strong predictive abilities (with Q^2 = 0. 64, R^2_{ncv} = 0.93, R^2_{pred} = 0.80 and Q^2 = 0. 65, R^2_{ncv} = 0.98, R^2_{pred} = 0.86, respectively). In addition, there was good concordance between these models, molecular docking, and MD results. Moreover, the MM-PBSA energy analysis reveals that the major driving force for ligand binding is the polar solvation contribution term. Hopefully, these models and the obtained findings could offer better understanding of the interaction mechanism of BVDV inhibitors as well as benefit the new discovery of more potent BVDV inhibitors.

KEYWORDS: *BVDV RdRp, 3D-QSAR, docking, molecular dynamics, MM-PBSA*

1. INTRODUCTION

Livestock (cattle, pigs, and sheep) infections by members of *Pestivirus* genus in the family Flaviviridae generate heavy losses in the global economy, and there is a strong need to develop effective and inexpensive antipestivirus agents.[1] Bovine viral diarrhea virus (BVDV), a prototype virus of the *Pestivirus* genus and a major pathogen of cattle, is also responsible for the economic loss of herds all over the world.[2] The prevention and control of BVDV infections therefore cause global economical concern.[3] In addition, BVDV, as a small enveloped, positive-stranded virus, comprise a single RNA genome, which is translated into a single polyprotein.[4] Since the RNA replication of BVDV RNA-dependent RNA polymerase (RdRp) can be initiated by a de novo mechanism without a primer and the RdRp of BVDV plays a critical role in viral replication,[5,6] BVDV RdRp therefore serves as one of the most promising drug targets for the development of a new anti-BVDV agent.

During the past eight years, many screening efforts have been devoted to target BVDV RdRp, leading to the identification and optimization of inhibitors with high potency. Up to now, a series of inhibitors with different structures have been collected from the literature[4,7−10] to inhibit the RdRp of BVDV, displaying various degrees of potency and selectivity. However, there is no specific antiviral drug that inhibits BVDV infection. Therefore, it is very important to develop antiviral lead compounds for treating expensive animals in breeding programs,[4] which specifically suppress the virus replication. Additionally, the development of new therapeutic alternatives for anti-BVDV is still difficult for researchers.

To facilitate the discovery of new drugs, computer-aided drug design (CADD) methods, including especially the three-dimensional quantitative structure activity relationship (3D-QSAR) method as the most significant applications[11,12] of chemometrics, provide valuable information for future design of novel inhibitors, which interact with a specific target.[13−15] Currently, employing comparative molecular field analysis (CoMFA)[16] and comparative molecular similarity indices analysis (CoMSIA)[17] approaches, a total of 65 benzimidazole scaffold-based derivatives as BVDV inhibitors[18−20] were collected to generate 3D-QSAR models. In addition, docking and molecular dynamics (MD) analysis were carried out to provide deep insight into the QSAR[21,22] and to explore the possible binding modes of these inhibitors at the bonding site of BVDV proteins.[23] The information derived from our work may be helpful for the future rational design of novel BVDV inhibitors with improved activity.

2. MATERIALS AND METHODS

2.1. Database Preparation and Splitting the Data Set. Presently, a series of 65 benzimidazole derivatives (Table S1) were investigated as BVDV inhibitors.[18−20] In order to use these in vitro EC_{50} values as dependent variables in the following QSAR investigations, all the inhibitory activities of these chemicals were

Received: March 5, 2016
Revised: June 7, 2016
Accepted: June 29, 2016
Published: June 29, 2016

DOI: 10.1021/acs.jafc.6b01067
J. Agric. Food Chem. 2016, 64, 5941−5950

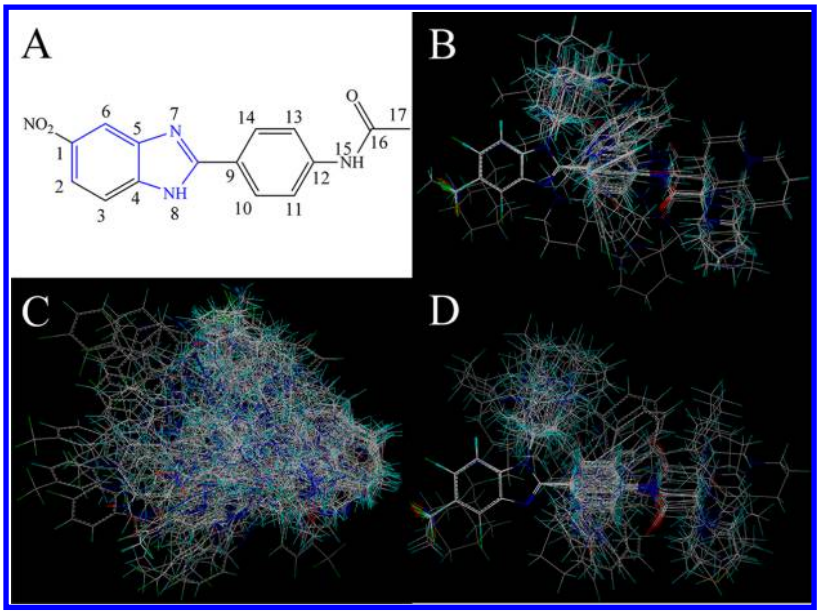

Figure 1. (A) Compound **39** was used as a template for alignments. The common substructure is shown in blue. Alignment-I, -II, and -III of all the compounds are shown in panels B, C, and D, respectively. Molecules are colored in white for common C, blue for N, red for O, yellow for S, and cyan for H atoms, respectively.

converted into the corresponding pEC_{50} ($-\log EC_{50}$) values. Since the division of the training and test sets for the whole data set is a crucial step for the construction of QSAR models, random selection, which is composed of rebuilding the QSAR models and assessing the resultant statistics, is a popular utilized method to evaluate the robustness of models.[24,25] In the current work, 65 compounds were divided into training and test sets in a proportion of 4:1 for generating and validating the model, respectively. To evaluate the predictive power of the models, the training and test set molecules were chosen randomly but their pEC_{50} values are uniformly distributed in terms of the value range of the whole set.

2.2. Molecular Modeling and Quantum Chemical Calculations. Using the SYBYL 6.9 software package,[26] molecular modeling work with the database alignment was carried out. To compute the partial atomic charges, Gasteiger–Hückel charges were used.

2.3. Alignment of Compounds. For generating the optimal 3D-QSAR model, we use three different alignment rules, i.e., alignment-I, -II, and -III. The first alignment strategy is an atom-based approach, where the highest active molecule **39** (Figure 1A) was selected as the template for all compounds. Then, applying the "align database" program in SYBYL6.9, the rest of the molecules were aligned to the common scaffold of molecule **39** to generate effective and reliable QSAR models (Figure 1B).

Alignment-II (Figure 1C) is a receptor-based approach, which was generated based on the derived conformation of template molecule derived from docking simulation. The third alignment rule (Figure 1D) is still a receptor-based approach. In this method, all conformations of the compounds were first derived from dock analysis, and then subjected to the process of alignment-I, i.e., the conformation of ligand **39** was also chosen as the template molecule to fit all others aligning the receptor-based conformations.

2.4. CoMFA and CoMSIA Descriptors. The descriptor fields of CoMFA were obtained by employing Tripos force field. For calculating the steric and electrostatic field energies, a steric probe, i.e., an sp^3 carbon with a van der Waals radius of 0.152 nm, and an electrostatic probe, i.e., a single positive +1 charge, were used, respectively. For CoMSIA analysis, the CoMSIA model was derived by five descriptor fields related to steric (S), electrostatic (E), hydrophobic (H), H-bond donor (D), and H-bond acceptor (A).[27]

2.5. Generation and Validation of QSAR Models. Using partial least-squares (PLS) analysis, the CoMFA and CoMSIA fields are linearly correlated with the activity values. The leave-one-out (LOO) method was adopted to carry out the initial cross-validation. In order to evaluate the predictive ability of obtained models, we performed the cross-validation analysis. Employing the cross-validated Q^2, the optimum number of components (ONC) with the lowest standard error of prediction (SEP) was generated. Using the ONC, the non-cross-validation analysis was performed, generating the final PLS regression models for 3D-QSAR. Through several statistical parameters like the non-cross-validated correlation coefficient (R^2_{ncv}), F value, and the standard error of estimate (SEE), the obtained non-cross-validation results were assessed. Besides, the cross-validated correlation coefficient (R^2_{pred}) evaluated the predictive capability of the derived CoMFA and CoMSIA models.

2.6. Docking. For validating the compound–target associations and generating the most probable binding conformation, GOLD (version 5.1) with a widely used genetic algorithm was performed. In order to predict the binding positions of ligand, we optimize the GOLD Score fitness function by considering van der Waals, H-bonding, and intramolecular strain.[28] In our studies, the X-ray crystal structure of the BVDV RdRp (PDB code 1S49) was obtained from the Protein Data Bank.[29,30]

2.7. Molecular Dynamics (MD). Using AMBER 10.0,[31] the MD simulations of all the molecules were carried out. Under periodic boundary conditions, the simulation process employed an NPT ensemble at 300 K.[32] The Berendsen thermostat approach was adopted to set the temperature to a constant. The values of 4.5×10^{-5} bar^{-1} for the isothermal compressibility were given, and the Parrinello–Rahman scheme was used to maintain the pressure at 1 bar.[33] To ensure the stability of the whole system, all simulations were run for 5 ns with a 2 fs time step.

2.8. MM–PBSA Calculation. Through the all-atom molecular mechanics and Poisson–Boltzmann solvation area (MM-PBSA) method,[34] a commonly used method in determining energetics on each complex system, the binding free energy of compounds to protein was calculated. The following equations were used to calculate the binding free energy:

$$\Delta G_{bind} = \Delta E_{MM} + \Delta G_{sol} \quad (1)$$

$$\Delta G_{MM} = \Delta E_{internal} + \Delta E_{electrostatic} + \Delta E_{vdw} \quad (2)$$

$$\Delta G_{sol} = \Delta G_{PB/GB} + \Delta G_{SA} \quad (3)$$

DOI: 10.1021/acs.jafc.6b01067
J. Agric. Food Chem. 2016, 64, 5941–5950

where ΔG_{MM} is the interaction energy computed with the molecular mechanics method and ΔG_{sol} is the solvation energy. ΔE_{MM} denotes the molecular mechanical free energy, which consists of van der Waals interaction energy (ΔE_{vdw}), the electrostatic interaction energy ($\Delta E_{electrostatic}$), and the internal energy of bonds, angles and torsions ($\Delta E_{internal}$). ΔG_{sol} encodes the solvation free energy, which is the sum of electrostatic solvation. Because of the negligible contribution of the entropy to the binding free energy to the same protein, which is described in many studies,[35,36] presently, the entropy contribution was not computed.

3. RESULTS

3.1. 3D-QSAR Models. To assess a QSAR model's reliability for activity prediction of unknown compounds, various statistical parameters containing the Q^2, R^2_{ncv}, SEE, ONC, R^2_{pred}, and F-statistic values were analyzed.[37] Generally speaking, a cross-validated $Q^2 > 0.5$ is considered as evidence of a 3D-QSAR model with satisfactory predictive capability.[38] Additionally, the foundation of a reliable QSAR model involves high R^2_{ncv} and F values as well as low SEE values.[39] Currently, to derive the reliable models, three alignment methods, i.e., alignment-I, -II, and -III, were adopted. The statistical results of the obtained QSAR models are summarized in Table 1. Clearly,

Table 1. Summary of CoMFA and CoMSIA Results

	alignment-I		alignment-II		alignment-III	
PLS statistics[a]	CoMFA	CoMSIA	CoMFA	CoMSIA	CoMFA	CoMSIA
Q^2	0.64	0.65	0.20	0.24	0.40	0.37
ONC	4	10	1	1	1	1
SEP	0.38	0.40	0.54	0.53	0.47	0.48
R^2_{ncv}	0.93	0.98	0.54	0.55	0.53	0.53
SEE	0.17	0.10	0.41	0.41	0.42	0.42
F	140.33	186.11	57.33	58.84	53.23	54.46
R^2_{pred}	0.80	0.85	−0.09	0.21	0.581	0.59
	Contribution (%)					
S	54.50	14.80	36.90	17.90	55.60	22.50
E	45.50	33.10	63.10	23.40	44.40	31.60
H		29.60		29.50		22.90
A		22.60		29.20		23.00

[a] Q^2 = cross-validated correlation coefficient using the LOO methods. R^2_{ncv} = non-cross-validated correlation coefficient. SEE = standard error of estimate. $F = R^2_{ncv}/(1 - R^2_{ncv})$. R^2_{pred} = predicted correlation coefficient for the test set of compounds. SEP = standard error of prediction. ONC = optimal number of components.

among all the CoMFA and CoMSIA models, alignment-II and -III led to statistically unacceptable models with $Q^2 < 0.5$, while alignment-I generated models with more significant statistical values, i.e., larger Q^2, R^2_{ncv}, F value, and R^2_{pred} and lower SEE values. Therefore, we mainly focused on alignment-I-based models, which were further used for the following discussion.

3.1.1. CoMFA Results. By analyzing the generated 3D-QSAR models, we found that, through a combinational use of S and E fields, the best CoMFA model was generated. The optimum number of components was 4 with Q^2 leave-one-out value 0.64 while the PLS analysis gave a good R^2_{ncv} value of 0.93, F = 140.33, and a low SEE of 0.17. These results demonstrate the stability and robustness of this model.

Currently, to validate the constructed 3D-QSAR model, 15 BVDV inhibitors in the test set were used. The predicted R^2_{pred} value for the test set from CoMFA was 0.80, indicating that this model has strong predictive capability. The radar correlation plot of the experimental values versus the predicted activities employing the training and test sets for the optimal CoMFA model is depicted in Figure S1. Clearly, a good accordance between the predicted pEC_{50} values and the actual pEC_{50} values was found in a tolerable error range. These statistical parameters suggest that, during the drug design process, the generated CoMFA model contour maps should be taken into consideration.

3.1.2. CoMSIA Results. For CoMSIA models, using five field descriptors, i.e., S, E, H, D, and A fields, all 31 possible combinations of descriptors were computed to build various CoMSIA models. Here, the combination of S, E, H, and A fields leads to the optimal CoMSIA result with larger Q^2, R^2_{ncv}, and R^2_{pred} and lower SEE values, which was used for the following discussion. Table 1 shows the statistical result of this CoMSIA model.

As shown in Table 1, the combination of S, E, H, and A gives a good LOO cross-validated Q^2 of 0.65 using 10 optimum components, indicating the strong ability of predicting the EC_{50} values of this model. In addition, a high R^2_{ncv} of 0.98 and a SEE value (0.10), as well as an F value (186.11), are obtained, presenting a good agreement of the actual and the predicted pEC_{50} values for the non-cross-validated model. The contribution fields of S, E, H, and A were shown to be 14.80%, 33.10%, 29.60%, and 22.60%, respectively.

Similar to the CoMFA model, 15 compounds in the same test set were used to test the reliabilities of the generated model. As shown in Table 1, an excellent value of 0.86 R^2_{pred} was obtained for the CoMSIA model, demonstrating its capability for accurately predicting the affinity of ∼86% compounds. Figure 2 shows the scattered plot of the predicted activity data versus the actual data with small variations for the training and test sets. The good correlations prove the robustness and good predictive ability of the optimal CoMSIA model.

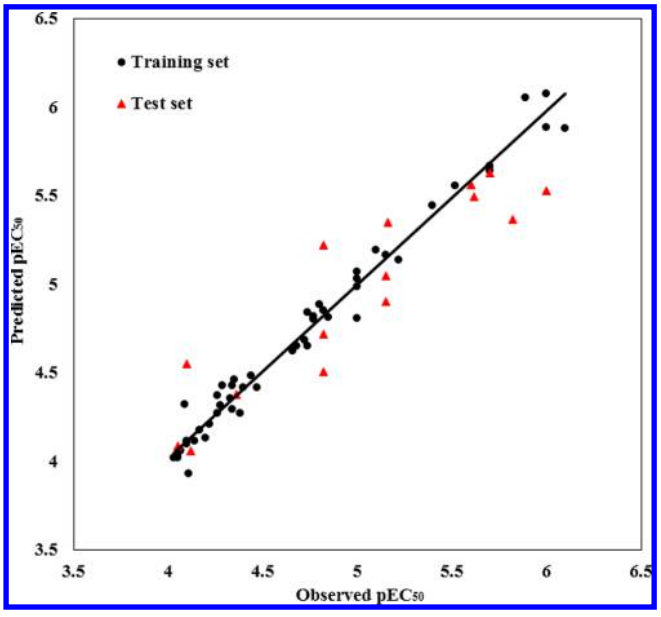

Figure 2. Ligand-based correlation plots of the predicted versus the actual pEC_{50} values using the training (filled black dot) and the test (filled red triangles) set compounds based on the CoMSIA model from random splitting.

DOI: 10.1021/acs.jafc.6b01067
J. Agric. Food Chem. 2016, 64, 5941−5950

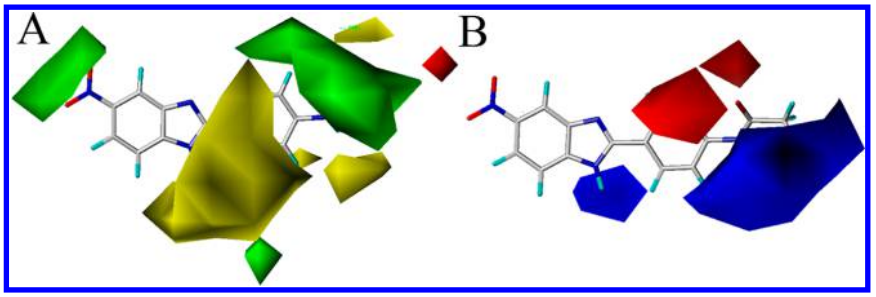

Figure 3. CoMFA StDev*Coeff contour maps put onto the most active molecule **39**. (A) Steric contour map. Green and yellow contours illustrate regions where steric bulk has favorable and unfavorable effects on the activity, respectively. (B) Electrostatic contour map in combination, in which blue contours indicate regions where electropositive groups increase the activity, while red contours indicate regions where electronegative groups increase the activity. The default values of 80% contribution for favored and 20% for disfavored regions were set for the visualization of the CoMFA contour maps.

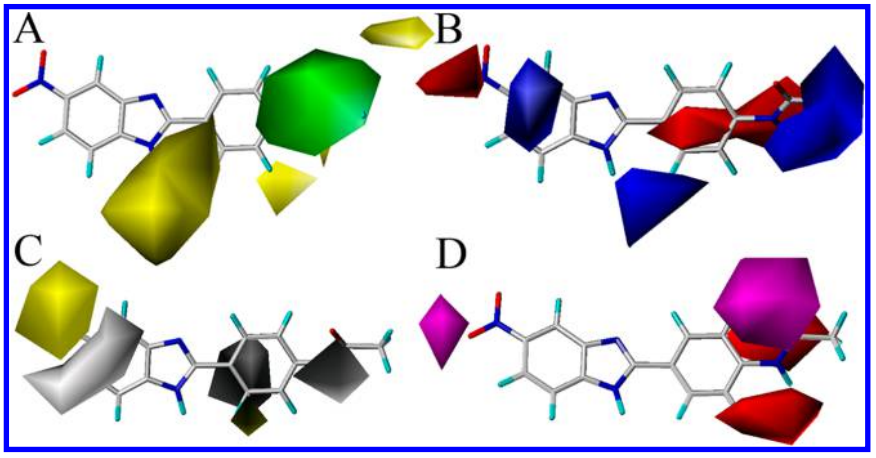

Figure 4. CoMSIA StDev*Coeff contour maps put onto the most active molecule **39**. (A) Steric contour map. Green and yellow contours illustrate regions where steric bulk has favorable and unfavorable effects on the activity, respectively. (B) Electrostatic contour map in combination, in which blue contours indicate regions where electropositive groups increase the activity, while red contours indicate regions where electronegative groups increase the activity. (C) Hydrophobic contour map. Yellow shows regions in which the introduction of hydrophobic groups is favored; white indicates regions where the introduction of hydrophobic groups is disfavored. (D) HB acceptor contour map. Purple shows regions where the introduction of H-accepting groups is favored; red indicates regions where the introduction of H-acceptors is disfavored. The default values of 80% contribution for favored and 20% for disfavored regions were set for the visualization of the CoMSIA contour maps.

3.2. Contour Map Analysis. For viewing the field effects on the target features, the 3D contour maps of the optimum CoMFA and CoMSIA models were constructed and analyzed, offering good insight into the new drug design.[40] To aid in visualization, the most active inhibitor (compound **39**) along with the CoMFA and CoMSIA contour maps is depicted in Figures 3 and 4, respectively.

In the case of the CoMFA model, Figure 3A depicts its steric contour maps. Green and yellow contours represent regions where bulky groups favor and disfavor the activity of inhibitors, respectively. As observed in Figure 3A, a large positive green isopleth around the $-CH_3CO$ and a little green contour near the $-NO_2$ show sterically favored positions, meaning that chemicals with bulky groups at these positions should present higher bioactivity than those without or with less bulky substituents in that location. For example, a comparison of compounds **27** and **33** shows that changing the group from $-CH_3CO$ to $-CH_3CH_2CO$ in this position might improve the activity. Moreover, compound **29** ($(CH_2)_4N-CH_2CO$) has relatively lower activity as compared to compound **45** ($CH_3N(CH_2CH_2)_2N-CH_2CO$), which might be partly due to the steric interaction. Additionally, compound **23** possessing a 5-NO_2 group has lower potency than compound **24** ($-COHCH_3$) possibly owing to the green isopleth. Also, a big yellow map near the benzimidazole, embedding positions 9−12 and the NH bridge at position 15, indicates that having big substituents in these sites is unfavorable for the activity.

The contour maps of electrostatic descriptor are presented in Figure 3B, where the blue and red regions suggest the preference of electropositive groups and electronegative substitutions, respectively. As a matter of fact, most of the excellent derivatives (**22**, **40**−**47**) possess electron-donating $-NH_2$, $-NHCH_3$, $-NCH_3CH_3$, and $-OCH_3$ groups around the $-CH_3CO$. As clearly observed from Figure 3B, a red contour with medium size at position 13 shows that molecules with electron-withdrawing substituents at this site have higher activity. Actually, those with highly electron-withdrawing N or O atoms at position 13 (**1**−**33**) are mostly inactive compounds, which is partly due to the presence of red contours around here.

By comparing with CoMFA model, the optimal CoMSIA model generated from our work not only computes the descriptors of steric and electrostatic fields but also utilizes the hydrophobic and HB acceptor fields to correlate with the activity of inhibitors. Figures 4A and 4B depict the steric and electrostatic contours of the CoMSIA model with favoring and disfavoring activity, respectively, which are nearly in accordance with the corresponding CoMFA contours (Figures 3A and 3B).

DOI: 10.1021/acs.jafc.6b01067
J. Agric. Food Chem. 2016, 64, 5941−5950

Thus, they are not discussed here, and we mainly discuss the CoMSIA hydrophobic contours and the H-bond acceptor contours below.

The hydrophobic contours of the CoMSIA model are presented in Figure 4C, where the yellow and gray areas suggest the favorable and unfavorable hydrophobic features, respectively. As clearly seen from Figure 4C, a yellow contour with optimal sized length around position 1 plays a significant role for increasing the inhibitory activity of the molecule, owing to the occupancy of hydrophobic groups. Moreover, trailed by the yellow region, one big gray contour observed in Figure 4C indicates that the benzimidazole ring with the optimal chain length is required attached to position 1, demonstrating the favor for hydrophilic groups at this location. Additionally, the gray maps with the optimal sized length presented around positions 10 and 16 suggest that the occupancy of hydrophobic substitutions will improve the activity. In fact, after comparing compounds **32**−**52** ($pEC_{50} > 5$), a pattern for the hydrophobic groups existing at these positions is found. On the contrary, the lower biological activities of compounds **1**−**3** ($pEC_{50} < 5$) are possibly due to the favored region of the hydrophilic groups.

In terms of the H-bond acceptor contour maps of the CoMSIA model, the purple and red regions displayed in Figure 4D represent the increased and decreased activity of chemicals with H-bond acceptor substituents, respectively. Clearly, a bulky favorable purple contour presented near the $-COCH_3$ of the position 16 moiety of compound **39** suggests the need for acceptor substitutions at this location to maintain the maximum potency of compounds. By comparing compounds **41** and **26**, a conclusion can be drawn that an addition of a H-bond acceptor group $-OCH_3$ at this position would generate a higher activity than $-NH_2$, which is exemplified by the improved activity from 4.79 to 6.00. In addition, two unfavorable red contours are found near the linker between positions 11 and 15, implying the increased inhibitory activity of molecules if they possess a H-bond donor substitute at these sites. This is in agreement with the observations between molecules **41** and **25**, in which compound **41**with an $-NH_2$ group displays an improved activity compared to compound **25** with the NO_2 in this position exhibiting significantly decreased potency.

3.3. Flexible Docking Analysis. The obtained compounds were docked into BVDV RdRp using the GOLD docking algorithm. Presently, all 65 chemicals were docked into the active site of protein 10 times for searching the possible binding conformation. The most potent compound **39** with the best pose was chosen for exploring the interaction mechanism of BVDV inhibitors and used for further analysis. Figure 5 shows the docking results of chemical **39** into the active site of the receptor with the key residues located at the binding pocket. In addition, Figure S2 depicts the binding gesture of compound **39** inside the active site cavity. Clearly, compound **39** is suitably situated at the GTP binding site, showing a good agreement with the X-ray crystal data of BVDV RdRp, supporting the validation of our docking study. The topmost pose of compound **39** is stabilized by hydrogen bonding and electrostatic interactions, as well as hydrophobic interactions with the residues at the binding pocket.

As shown in Figure 5, fitting compound **39** into the difference electron density map, its orientation is supported by a basic environment containing the phosphate groups (His499, Arg517, Ly525, Arg529) and a polar environment including the ribose OH groups (Ser548) as well as the hydrophobic environment around the guanine base (Phe549, Met552, Tyr553, Ile522), which is also almost similar to the GTP binding site in BVDV RdRp.[29,30] From docking studies, we observed that compound **39** and GTP lie in the same pocket of BVDV RdRp, presenting the contributions of key active-site residues to the ligand−receptor interaction. The binding interactions showed a good binding affinity for interaction with the BVDV RdRp active binding site.

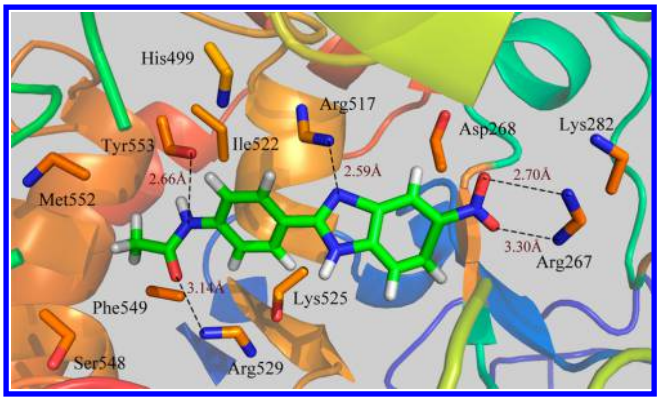

Figure 5. Stereo view of docking interactions of compound **39** with active site amino acid residues of BVDV RdRp.

In addition to the above interactions with active-site residues, hydrogen bonding analyses are also carried out in our docking study. It is observed from Figure 5 that the core of the ligand is anchored in the active site through four hydrogen-bonding interactions with the BVDV RdRp. In detail, the oxygen and nitrogen atoms in positions 15 and 16 participate in the hydrogen bonding with Arg529 (−O···HN, 3.14 Å) and Tyr553 (−O···HN, 2.66 Å). These hydrogen bonds are perfectly filled in the center of the BVDV RdRp pocket, and play essential roles in improving the inhibitors' activity. Additionally, the nitrogen atom in the scaffold of benzimidazole ring bound in the hydrogen bonding with Arg517 at a distance of 2.59 Å, showing a good concordance with the results of Rossmann et al.[30] In addition, the $-NO_2$ group at the terminal of compound **39** solidly formed two hydrogen bonds with the Arg267 (−O···HN, 2.70 and 3.03 Å).

Moreover, in order to further explore the binding position of the BVDV derivatives, the binding modes of the lowest active compound **64** and medium affinity inhibitor **29** were also investigated (Figure S3). As demonstrated in Figure S3A, molecule **64** fitted into the binding cavity which consists of His499, Ser498, Arg285, Asp268, Arg267, Arg529, Lys525, Ile522, Ser548, Phe549, Met552, and Tyr553. Additionally, there are two potential H-bonds formed by compound **64** with Arg529. Through a comparison of the binding site of chemical **39**, we find that compound **64** appears at almost the same binding site as compound **39**, and when a big group is introduced, the binding mode changes clearly affect the binding affinity. Due to the strong steric hindrance of this substituent, the H-bond is broken, and the nitrogen atom of the substituent in turn forms two H-bonds with residue Arg529. This may be the reason that compound **64** is the least active molecule.

Figure S3B shows the binding conformation of compound **29**. Obviously, hydrogen-bonding and hydrophobic interactions with particular active-site residues are crucial for the stabilization of the docked pose of the medium active molecule **29** into BVDV RdRp. In total, there are three H-bonds that were found between the ligand and residues Arg529 and Ser498. Compared with the binding mode of compound **39**, we

DOI: 10.1021/acs.jafc.6b01067
J. Agric. Food Chem. 2016, 64, 5941−5950

observed that both inhibitors adopted the same binding pocket and the substituent at the position 17 affects the binding energies. This is not surprising because both compounds contain the same scaffold and similar substituents. However, when this position of compound **39** was substituted by −OCH3, the binding energies increased remarkably, owing to the hydrophobic interactions with residues Phe549, Met552, Tyr553, and Ile522. Therefore, molecular optimization near this region would further improve bioactivity.

Taken together, all the findings yield valuable insights into the molecular mechanisms of the BVDV inhibitors, which will facilitate medicinal chemists in identifying the scaffolds surpassing the congeneric series of chemical space used for a general QSAR methodology.[41]

3.4. MD Analysis. To assess the reasonability of the binding mode predicted by GOLD, the initial ligand geometries generated from the docking model were used to perform MD protocols. Herein, a 5 ns MD simulation was carried out to investigate the molecular interactions involved in ligand **39** and the receptor, with main emphasis on exploring the conformational changes occurring in the obtained complex.

Additionally, to check the dynamic stability of the simulated system, the root-mean-square deviation (RMSD) of the MD trajectories for the initial complex was calculated. Figure 6A

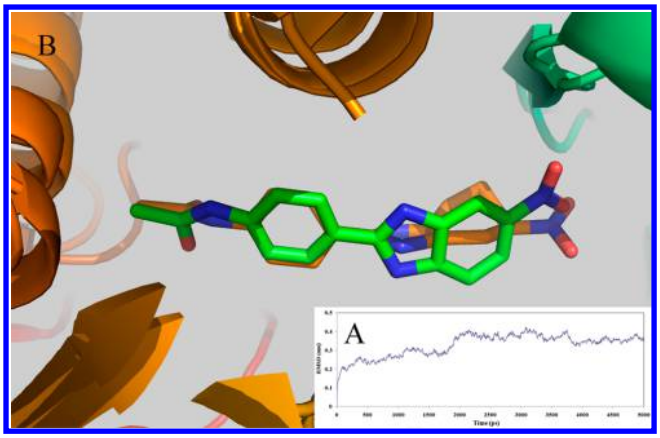

Figure 6. (A) View of superimposed backbone atoms of the average structure for the MD simulations and the initial structure of the docking for the complex. (B) Plot of the root-mean-square deviation (RMSD) of docked complex/ligand versus the MD simulation time in the MD-simulated structures. Compound **39** is represented as carbon chain in green for the initial complex and carbon chain in maroon for the average structure, respectively.

depicts the RMSDs of the system simulation for the BVDV RdRp complex. Clearly, the RMSD value for the protein−ligand complex trajectory reaches 1.6 to 3 Å from initial to 1.1 ns and undergoes a conformational change during the MD simulation. After 2 ns, the RMSD value attains a plateau about 4 Å, suggesting that the model thereafter is in equilibrating state from 1.1 to 2 ns. Besides, it is observed that, after 2 ns of simulation, a clear metastable conformation for the molecular system was found.

Furthermore, a superimposition of the initial structure from docking and the average structure of the complex for the last 1 ns from MD simulations is shown in Figure 6B. Obviously, the average structure and the initial docked structure of the ensemble are superimposed well. In addition, after a certain time, more consistency in conformation of the docked complex of compound **39** was observed during the MD process, which indicates that the ligand is stable during the course of simulation.

Since hydrogen-bonding interactions deeply affect the specificity, adsorption, and metabolization of drugs, they play important roles in the development of drug design.[42] For exploring the positional conformational variations in the ligand of the binding pocket, hydrogen-bonding interactions with the main native contacts in both MD and docking simulations were compared (Figure 7).[43] As seen from Figure 7, a total of three

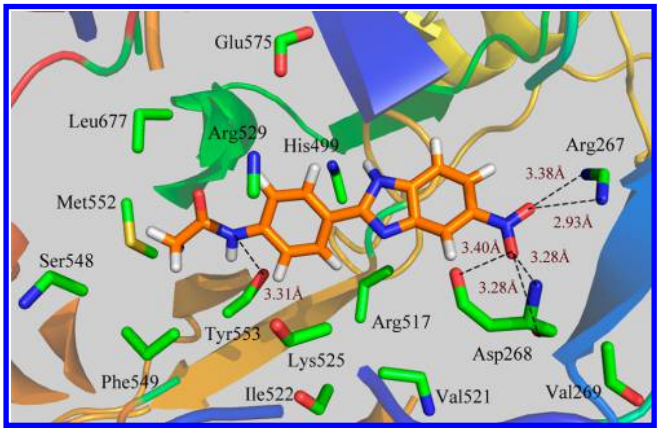

Figure 7. Plot of the MD-simulated structures of the binding site with compound **39**. H-bonds are shown as dotted red lines; active site amino acid residues are represented as sticks.

H-bonds appeared in both simulation systems for the protein−ligand complex. In docking simulation, a backbone H-bond is observed with Tyr553, whereas in MD simulation, a side chain H-bond is noted with the same residue. In addition, the NH groups of Arg267 form two stable H-bonds with the ligand in docking study, showing high occupancy, which are consistent with the docking results (Table S2). Moreover, in MD simulation, compound **39** forms three stable hydrogen bonds with Asp268. Similar to the results obtained from docking, the majority of crucial residues in the binding site including Phe549, Tyr553, Ile522, Lys525, Arg517, Val521, Asp268, Val269, Arg267, His499, Arg529, Glu575, Leu677, Met552, and Ser548 are observed during MD simulation, showing the reliability of our docking model. Actually, there are some small changes existing in the MD simulation, but the conformation of the ligand in the binding pocket is still stable, indicating the rationality and reasonability of our docking study. All these findings derived from our dry lab work would be helpful in designing novel BVDV inhibitors. The key structural features with the requirement for improving the activity of chemicals are shown in Figure S4.

3.5. Binding Free Energy Component Analysis. With an attempt to evaluating the relationship between the biological activities of inhibitors with their binding affinities, we calculated the binding free energy of compound **39** with the RdRp of BVDV employing the MM-PBSA approach. The MM-PBSA is composed of four terms, i.e., the van der Waals interaction energy (ΔE_{vdw}), the electrostatic energy ($\Delta E_{electrostatic}$), the nonpolar solvation free energy (ΔG_{SA}), and the polar solvation free energy ($\Delta G_{PB/GB}$). Table 2 shows the binding free energy results with the detailed contribution of each energy component.

DOI: 10.1021/acs.jafc.6b01067
J. Agric. Food Chem. 2016, 64, 5941−5950

Table 2. Contributions of Various Energy Components to the Binding Free Energy (kcal mol^{-1}) for the Studied Inhibitor with BVDV[a]

	receptor		ligand		complex		delta	
component	mean	std	mean	std	mean	std	mean	std
ΔE_{vdw}	−4783.33	3.71	−1.08	0.13	−4809.17	3.74	−24.76	0.20
$\Delta E_{electrostatic}$	−40717.37	10.08	−12.21	0.23	−40772.15	10.17	−42.55	0.41
$\Delta G_{PB/GB}$	−9271.96	8.21	−27.63	0.07	−9236.90	8.18	62.69	0.50
ΔG_{SA}	157.77	0.15	1.90	0.00	157.38	0.15	−2.30	0.02
$\Delta E_{gas}(E_{MM})$	−45500.71	10.76	−13.31	0.24	−45581.32	10.80	−67.31	0.45
ΔG_{sol}	−9114.19	8.17	−25.72	0.07	−9079.52	8.14	60.40	0.50
ΔG_{bind}	−54614.89	7.65	−39.03	0.23	−54660.84	7.65	−6.91	0.37

[a] ΔE_{vdw}, energies shown as contributions from van der Waals energy; $\Delta E_{electrostatic}$, electrostatic energy; ΔG_{PB} is the polar solvation energy with the PB model; ΔG_{bind} is the sum of ΔE_{vdw} + $\Delta E_{electrostatic}$ + $\Delta G_{PB/GB}$ + ΔG_{SA}; delta is equal to mean (complex) − [mean (ligand) + mean (receptor)]; std, standard error of mean values.

As shown in Table 2, the total binding free energies of the binding system in drug−receptor complex simulations is −6.91 kcal·mol^{-1}, revealing that compound **39** prefers binding to BVDV RdRp. Moreover, a further observation of the individual free energy component suggests the important contributions of the van der Waals (−24.76) and electrostatic (−42.55) interactions in the ligand-binding system. Additionally, the polar interaction terms ($\Delta E_{electrostatic}$ + $\Delta G_{PB/GB}$) made a slightly favorable contribution to the ligand−protein complex. With respect to the nonpolar interaction contributions (ΔE_{vdw} + ΔG_{SA}), they offer the dominant driving forces for the binding, indicating that the association of the receptor−ligand complex is predominantly driven by the highly favorable nonpolar interaction contribution rather than by the polar ones.

4. DISCUSSION

4.1. Comparing Contours with MD Results. For testing the reliability of the built models, the contour maps were used for a comparison with the MD results. As depicted in Figures 3A and 4A, the large positive yellow contour maps of the CoMFA and CoMSIA models suggest that the bulky/steric groups around the −CH_3CO are not favored, which coincides well with the results derived from MD, where the large substitutions added here will lead to a decreased activity. Actually, MD studies have demonstrated that there are many residues including Arg529, His499, and Tyr553 at this region, leading to a small volume of the binding pocket. Therefore, too large groups introduced here may result in a steric clash, which is in accordance with the steric yellow contours of the previous CoMFA and CoMSIA models. In electrostatic contour maps, it is worth mentioning that several electropositive residues including His499, Arg529, and Arg517 are around position 15, indicating that this region is favorable for electronegative groups, which is in good accordance with the electrostatic blue contour by CoMFA and CoMSIA analysis (shown in Figures 3B and 4B). Similarly, the binding pocket also has a small quantity of electronegative charge at position 9 due to the amino acid residue Asp268, thus forming a favorable interaction with the negatively charged substitution of the ligand, which can be deduced from the blue contours seen in the above CoMFA and CoMSIA analysis.

In addition, Figure 7 shows that position 1 points toward the hydrophobic binding pocket formed by Val521 and Val269 residues. As a matter of fact, the groups at this position were almost hydrophobic, which may explain the presence of yellow contour maps in the above CoMSIA study. Moreover, the H-bond acceptor contours of CoMSIA correlate well with the H-bond interactions involved in affecting the binding and activity of ligand. In detail, the oxygen atom of −NO_2 at the terminal of the compound **39** solidly forms five bonds (Figure 7) with the Arg267 (−O···HN, 3.38 and 2.93 Å) and Asp268 (−O···HN, 3.38 and 2.93 Å), which is strongly supported by the purple contour at this position as observed from the previous CoMSIA model (Figure 4D).

Overall, during MD simulation, all the steric, electrostatic, hydrophobic, and H-bond acceptor interactions between the ligand and BVDV RdRp are in good agreement with the contour maps described previously, suggesting the reasonability of the QSAR models generated presently. All these results may offer useful information for the discovery of new potent BVDV inhibitors in the future.

4.2. Comparison of Binding Mode Analysis. To further explore the binding mode of the BVDV inhibitors and determine whether a similar mechanism of BVDV RdRp existed, docking procedure was carried out with the developed BVDV inhibitors. First, we directly compare the binding site of compound **39** with the crystal structure of the BVDV RdRp bound to GTP. Then, the findings of previous works were compared with the current results. All obtained results could provide useful insights for developing novel BVDV inhibitors with improved potency.

4.2.1. Comparison with the Crystal Structure of the BVDV RdRp Bound to GTP. By comparing the docking results of compound **39** with the crystal structure of the BVDV RdRp bound to GTP, we found that both ligands are deeply located inside the BVDV RdRp pocket and their binding modes are almost similar, proving the reasonability of our docking process. As seen from Figure S5, like chemical **39** in the docking study, the binding site for the X-ray crystal data of compound GTP was also enclosed in the difference electron density map, which consists of the phosphate groups (His499, Arg517, Ly525, and Arg529), a polar environment including the ribose OH groups (Ser498), and the hydrophobic environment around the guanine base (Tyr581). Additionally, for understanding the flexibilities of BVDV RdRp and exploring the protein−ligand interactions, the H-bonds for ligands **39** and GTP were compared as well. In Figure S5, a H-bond formed with Arg517 was observed in X-ray crystallography of the molecule with the BVDV protein, which coincides well the results in the docking study. Due to the difference of the structure of the two compounds and the strong steric hindrance of the −$NHCOCH_3$ group near positions 15, 16, and 17 in our docking result, compound **39** has only a slight conformational drift compared with the X-ray crystal data of compound GTP.

DOI: 10.1021/acs.jafc.6b01067
J. Agric. Food Chem. 2016, 64, 5941−5950

Moreover, four new H-bonds were formed in the docking study (Figure 5). In detail, the oxygen and nitrogen atoms of the ligand participate in the hydrogen bonding with Arg529 and Tyr553 and the $-NO_2$ group of compound **39** solidly forms two hydrogen bonds with the Arg267. Although the difference of the H-bonds between the compound **39** and GTP of the two binding modes is small, the orientation of the ligand still can be observed. Therefore, the almost similar orientation of the ligands in the binding cavity for both the current work and the X-ray crystal data once again demonstrates the reliability of our docking model.

4.2.2. Comparison with Five Known BVDV Inhibitors. Until now, there are several docking reports on BVDV RdRp receptor, making a great contribution for the exploitation and optimization of small-molecule inhibitors with high potency. As far as we know, five kinds of BVDV inhibitors including BPIP, LZ37, TSC, AG110, and γ-carboline based on the molecule modeling were reported in recent literature and their putative binding sites were used for a comparison with our docking results. Figure S6 summarizes the structures of these molecules, and the major structural features impacting the activity drawn by them are summarized in Table S3, where the similarities and differences of these studies are easily observed.

Obviously, four binding modes including Phe224, Glu291, Asn264, and Ala392 positions are found in Table S3. In fact, these binding modes share common characteristics with the prominent hydrogen-bonding interactions, and most of the ligands occupy approximately the same area in the hydrophobic domains. In terms of the differences in these binding modes, they are mainly the residues which participate in the hydrogen-bonding and hydrophobic interactions.

In the case of the first binding mode, molecular docking studies have revealed that Phe224 is situated in a small cavity near the top of the finger domain region of the BVDV RdRp, forming possible interactions with the inhibitor BPIP.[44,49] In the work of Paeshuyse et al.,[44] the hydrophobic region of BPIP interacting with residues Ala221, Ala222, and Phe224 and an H-bond between Phe224 and the imidazole ring of BPIP are observed. Additionally, the γ-carboline formed a H-bond with Ala392 and an aromatic-ring stacking interaction with Phe224.[45] Docking of LZ37 close to Phe224 revealed the important roles of the hydrophobic and hydrogen-bonding interactions in the binding site.[46] With regard to the Glu291 position, docking of AG110 into the receptor showed the hydrophobic contacts of AG110 with Leu225, Leu244, Ile254, Lys255, and Tyr257.[47] Moreover, a H-bond was formed by the side chain of Glu291with the N7 of AG110.[47] As a result, AG110 was stabilized and located between the side chains and the hydrophobic interactions.

For the Asn264 position, the docking of TSC close to Asn264 presented several H-bond interactions between the BVDV RdRp and TSC.[48] In detail, a total of four H-bonds were found between the TSC and the residues Asn264, Glu265, and Lys266,[48] indicating that the H-bonds are essential in determining the potency of the TSC. Moreover, by docking TSC into BVDV RdRp, a similar interaction with the Asn264 position was observed in the binding mode. The thiocarbonyl group of TSC is located at the binding pocket which contains the protein residues Phe165 and Ala392, and two strong H-bonds are observed between residues Thr152, Thr160, and the N4 of the thiosemicarbazone group.[48] All these interactions are therefore required for the high-affinity binding.

In summary, by a comparison of the four binding modes with our docking study, a similar interaction mechanism was found among them, indicating that they complement each other and validate our generated models. All the findings could give a new strategy for the future design of novel inhibitors with high biological activities.

4.3. Design of New BVDV Inhibitors. Evaluating a QSAR model is not only by how well it fits the data, but more importantly by how well it predicts data. The contour maps, docking studies, and MD results offer region-specific substituents on the scaffolds of compounds, which are crucial for improving the activity of BVDV inhibitors. Based on this information, we tried to design a set of new compounds in silico, with steric, electrostatic, hydrophobic, and HB acceptor substitutions in their favored regions. From molecular modeling we know that appropriate substituents mainly in regions 1−3 (Figure S4) are favored for the activity. Therefore, we focused the modifications on regions 1−3 in the reference molecule **39** to design potent BVDV inhibitors. Interestingly, eight molecules (No. ND01−08, Figure S7) showed potent inhibitory activity against BVDV RdRp. As shown in Figure S7, it is obvious that all eight designed molecules show better pEC_{50} than that of the reference molecule **39**.

Since our current study mainly concentrates on the *in silico* investigation of the SAR of benzimidazole derivatives as BVDV inhibitors and the exploration of their possible inhibition mechanism, further experimental evaluation for validating the inhibitory activity of these novel-designed chemicals is needed.

■ ASSOCIATED CONTENT

Supporting Information

The Supporting Information is available free of charge on the ACS Publications website at DOI: 10.1021/acs.jafc.6b01067.

BVDV inhibitor structures, pEC_{50} values, H bond analysis, and BVDV study details (PDF)

■ AUTHOR INFORMATION

Corresponding Author

*Tel: +86-029-87092262. E-mail: yh_wang@nwsuaf.edu.cn.

Author Contributions

§J.W. and Y.Y. are co-first authors.

Funding

Financial support from the National Natural Science Foundation of China (No. 11201049, 10801025, and 30973590) and the National High Technology Research and Development Program ("863") of China (No. 2009AA02Z205).

Notes

The authors declare no competing financial interest.

■ REFERENCES

(1) Tonelli, M.; Vettoretti, G.; Tasso, B.; Novelli, F.; Boido, V.; Sparatore, F.; Busonera, B.; Ouhtit, A.; Farci, P.; Blois, S. Acridine derivatives as anti-BVDV agents. *Antiviral Res.* **2011**, *91*, 133−141.

(2) Gao, Y.; Zhao, X.; Sun, C.; Zang, P.; Yang, H.; Li, R.; Zhang, L. A transgenic ginseng vaccine for bovine viral diarrhea. *Virol. J.* **2015**, *12*, 1−7.

(3) Xue, W.; Zhang, S.; Minocha, H. C. Characterization of a putative receptor protein for bovine viral diarrhea virus. *Vet. Microbiol.* **1997**, *57*, 105−118.

DOI: 10.1021/acs.jafc.6b01067
J. Agric. Food Chem. 2016, 64, 5941−5950

(4) Chai, H.; Lim, D.; Chai, H.; Jung, E. Molecular modeling of small molecules as BVDV RNA-dependent RNA polymerase allosteric inhibitors. *Bull. Korean Chem. Soc.* **2013**, *34*, 837−850.
(5) Baharuddin, A.; Amir Hassan, A.; Chye Sheng, G.; Bakhtiar Nasir, S.; Othman, S.; Yusof, R.; Othman, R.; Abdul Rahman, N. Current approaches in antiviral drug discovery against the Flaviviridae family. *Curr. Pharm. Des.* **2014**, *20*, 3428−3444.
(6) Malet, H.; Massé, N.; Selisko, B.; Romette, J.-L.; Alvarez, K.; Guillemot, J. C.; Tolou, H.; Yap, T. L.; Vasudevan, S. G.; Lescar, J. The flavivirus polymerase as a target for drug discovery. *Antiviral Res.* **2008**, *80*, 23−35.
(7) Puerstinger, G.; Paeshuyse, J.; De Clercq, E.; Neyts, J. Antiviral 2, 5-disubstituted imidazo [4, 5-c] pyridines: From anti-pestivirus to anti-hepatitis C virus activity. *Bioorg. Med. Chem. Lett.* **2007**, *17*, 390−393.
(8) Tonelli, M.; Boido, V.; La Colla, P.; Loddo, R.; Posocco, P.; Paneni, M. S.; Fermeglia, M.; Pricl, S. Pharmacophore modeling, resistant mutant isolation, docking, and MM-PBSA analysis: Combined experimental/computer-assisted approaches to identify new inhibitors of the bovine viral diarrhea virus (BVDV). *Bioorg. Med. Chem.* **2010**, *18*, 2304−2316.
(9) Giliberti, G.; Ibba, C.; Marongiu, E.; Loddo, R.; Tonelli, M.; Boido, V.; Laurini, E.; Posocco, P.; Fermeglia, M.; Pricl, S. Synergistic experimental/computational studies on arylazoenamine derivatives that target the bovine viral diarrhea virus RNA-dependent RNA polymerase. *Bioorg. Med. Chem.* **2010**, *18*, 6055−6068.
(10) Sako, K.; Aoyama, H.; Sato, S.; Hashimoto, Y.; Baba, M. γ-Carboline derivatives with anti-bovine viral diarrhea virus (BVDV) activity. *Bioorg. Med. Chem.* **2008**, *16*, 3780−3790.
(11) Wang, J.; Li, Y.; Yang, Y.; Zhang, J.; Du, J.; Zhang, S.; Yang, L. Profiling the interaction mechanism of indole-based derivatives targeting the HIV-1 gp120 receptor. *RSC Adv.* **2015**, *5*, 78278−78298.
(12) Wang, J.; Li, Y.; Yang, Y.; Zhang, S.; Yang, L. Profiling the Structural Determinants of Heteroarylnitrile Scaffold-Based Derivatives as Falcipain-2 Inhibitors by In Silico Methods. *Curr. Med. Chem.* **2013**, *20*, 2032−2042.
(13) Guariento, S.; Bruno, O.; Fossa, P.; Cichero, E. New insights into PDE4B inhibitor selectivity: CoMFA analyses and molecular docking studies. *Mol. Diversity* **2016**, *20*, 77−92.
(14) Cichero, E.; Fossa, P. Docking-based 3D-QSAR analyses of pyrazole derivatives as HIV-1 non-nucleoside reverse transcriptase inhibitors. *J. Mol. Model.* **2012**, *18*, 1573−1582.
(15) Cichero, E.; Buffa, L.; Fossa, P. 3, 4, 5-Trisubstituted-1, 2, 4−4H-triazoles as WT and Y188L mutant HIV-1 non-nucleoside reverse transcriptase inhibitors: docking-based CoMFA and CoMSIA analyses. *J. Mol. Model.* **2011**, *17*, 1537−1550.
(16) Zou, X.-J.; Lai, L.-H.; Jin, G.-Y.; Zhang, Z.-X. Synthesis, fungicidal activity, and 3D-QSAR of pyridazinone-substituted 1, 3, 4-oxadiazoles and 1, 3, 4-thiadiazoles. *J. Agric. Food Chem.* **2002**, *50*, 3757−3760.
(17) Huang, M.-Z.; Luo, F.-X.; Mo, H.-B.; Ren, Y.-G.; Wang, X.-G.; Ou, X.-M.; Lei, M.-X.; Liu, A.-P.; Huang, L.; Xu, M.-C. Synthesis and herbicidal activity of isoindoline-1, 3-dione substituted benzoxazinone derivatives containing a carboxylic ester group. *J. Agric. Food Chem.* **2009**, *57*, 9585−9592.
(18) Tonelli, M.; Paglietti, G.; Boido, V.; Sparatore, F.; Marongiu, F.; Marongiu, E.; La Colla, P.; Loddo, R. Antiviral Activity of Benzimidazole Derivatives. I. Antiviral Activity of 1-Substituted-2[(Benzotriazol-1/2-yl) methyl] benzimidazoles. *Chem. Biodiversity* **2008**, *5*, 2386−2401.
(19) Tonelli, M.; Simone, M.; Tasso, B.; Novelli, F.; Boido, V.; Sparatore, F.; Paglietti, G.; Pricl, S.; Giliberti, G.; Blois, S. Antiviral activity of benzimidazole derivatives. II. Antiviral activity of 2-phenylbenzimidazole derivatives. *Bioorg. Med. Chem.* **2010**, *18*, 2937−2953.
(20) Tonelli, M.; Novelli, F.; Tasso, B.; Vazzana, I.; Sparatore, A.; Boido, V.; Sparatore, F.; La Colla, P.; Sanna, G.; Giliberti, G. Antiviral activity of benzimidazole derivatives. III. Novel anti-CVB-5, anti-RSV and anti-Sb-1 agents. *Bioorg. Med. Chem.* **2014**, *22*, 4893−4909.
(21) Cichero, E.; D'Ursi, P.; Moscatelli, M.; Bruno, O.; Orro, A.; Rotolo, C.; Milanesi, L.; Fossa, P. Homology modeling, docking studies and molecular dynamic simulations using graphical processing unit architecture to probe the type-11 phosphodiesterase catalytic site: a computational approach for the rational design of selective inhibitors. *Chem. Biol. Drug Des.* **2013**, *82*, 718−731.
(22) Cichero, E.; Ligresti, A.; Allarà, M.; di Marzo, V.; Lazzati, Z.; D'Ursi, P.; Marabotti, A.; Milanesi, L.; Spallarossa, A.; Ranise, A. Homology modeling in tandem with 3D-QSAR analyses: a computational approach to depict the agonist binding site of the human CB2 receptor. *Eur. J. Med. Chem.* **2011**, *46*, 4489−4505.
(23) Ghasemi, J. B.; Nazarshodeh, E.; Abedi, H. Molecular docking, 2D and 3D-QSAR studies of new indole-based derivatives as HCV-NS5B polymerase inhibitors. *J. Iran. Chem. Soc.* **2015**, *12*, 1789−1799.
(24) Ambure, P.; Roy, K. Exploring structural requirements of leads for improving activity and selectivity against CDK5/p25 in Alzheimer's disease: an in silico approach. *RSC Adv.* **2014**, *4*, 6702−6709.
(25) Vesanto, J.; Alhoniemi, E. Clustering of the self-organizing map. *IEEE Trans. Neural Network* **2000**, *11*, 586−600.
(26) Good, A. C.; Hermsmeier, M. A. Measuring CAMD technique performance. 2. How "druglike" are drugs? Implications of random test set selection exemplified using druglikeness classification models. *J. Chem. Inf. Model.* **2007**, *47*, 110−114.
(27) Kothandan, G.; Gadhe, C. G.; Madhavan, T.; Cho, S. J. Binding site analysis of CCR2 through in silico methodologies: Docking, CoMFA, and CoMSIA. *Chem. Biol. Drug Des.* **2011**, *78*, 161−174.
(28) *GOLD User Guide & Tutorials*; CCDC Software Ltd: 2005; http://www.ccdc.cam.ac.uk/support/documentation/gold/4_0/gold/toc.html, 27/01/**2012**.
(29) Westbrook, J.; Feng, Z.; Chen, L.; Yang, H.; Berman, H. M. The protein data bank and structural genomics. *Nucleic Acids Res.* **2003**, *31*, 489−491.
(30) Choi, K. H.; Groarke, J. M.; Young, D. C.; Kuhn, R. J.; Smith, J. L.; Pevear, D. C.; Rossmann, M. G. The structure of the RNA-dependent RNA polymerase from bovine viral diarrhea virus establishes the role of GTP in de novo initiation. *Proc. Natl. Acad. Sci. U. S. A.* **2004**, *101*, 4425−4430.
(31) Kwon, Y. D.; Finzi, A.; Wu, X.; Dogo-Isonagie, C.; Lee, L. K.; Moore, L. R.; Schmidt, S. D.; Stuckey, J.; Yang, Y.; Zhou, T. Unliganded HIV-1 gp120 core structures assume the CD4-bound conformation with regulation by quaternary interactions and variable loops. *Proc. Natl. Acad. Sci. U. S. A.* **2012**, *109*, 5663−5668.
(32) Parrinello, M.; Rahman, A. Polymorphic transitions in single crystals: A new molecular dynamics method. *J. Appl. Phys.* **1981**, *52*, 7182−7190.
(33) Lin, J.-H.; Perryman, A. L.; Schames, J. R.; McCammon, J. A. Computational drug design accommodating receptor flexibility: the relaxed complex scheme. *J. Am. Chem. Soc.* **2002**, *124*, 5632−5633.
(34) Kollman, P. A.; Massova, I.; Reyes, C.; Kuhn, B.; Huo, S.; Chong, L.; Lee, M.; Lee, T.; Duan, Y.; Wang, W. Calculating structures and free energies of complex molecules: combining molecular mechanics and continuum models. *Acc. Chem. Res.* **2000**, *33*, 889−897.
(35) Zhou, Z.; Madrid, M.; Evanseck, J. D.; Madura, J. D. Effect of a bound non-nucleoside RT inhibitor on the dynamics of wild-type and mutant HIV-1 reverse transcriptase. *J. Am. Chem. Soc.* **2005**, *127*, 17253−17260.
(36) Zhao, Y.; Li, W.; Zeng, J.; Liu, G.; Tang, Y. Insights into the interactions between HIV-1 integrase and human LEDGF/p75 by molecular dynamics simulation and free energy calculation. *Proteins: Struct., Funct., Genet.* **2008**, *72*, 635−645.
(37) Malla, P.; Kumar, R.; Kumar, M. Validation of Formylchromane Derivatives as Protein Tyrosine Phosphatase 1B Inhibitors by Pharmacophore Modeling, Atom-Based 3D-QSAR and Docking Studies. *Chem. Biol. Drug Des.* **2013**, *82*, 71−80.
(38) Wang, J.; Li, F.; Li, Y.; Yang, Y.; Zhang, S.; Yang, L. Structural features of falcipain-3 inhibitors: an in silico study. *Mol. BioSyst.* **2013**, *9*, 2296−2310.
(39) AbdulHameed, M. D. M.; Hamza, A.; Liu, J.; Zhan, C.-G. Combined 3D-QSAR modeling and molecular docking study on

DOI: 10.1021/acs.jafc.6b01067
J. Agric. Food Chem. 2016, 64, 5941−5950

indolinone derivatives as inhibitors of 3-phosphoinositide-dependent protein kinase-1. *J. Chem. Inf. Model.* **2008**, *48*, 1760−1772.
(40) Lu, X.; Zhao, L.; Xue, T.; Zhang, H. Design of novel focal adhesion kinase inhibitors using 3D-QSAR and molecular docking. *Med. Chem. Res.* **2014**, *23*, 1976−1997.
(41) Nair, P. C.; Sobhia, M. E. Fingerprint directed scaffold hopping for identification of CCR2 antagonists. *J. Chem. Inf. Model.* **2008**, *48*, 1891−1902.
(42) Gupta, M. K.; Misra, K. Atom-based 3D-QSAR, molecular docking and molecular dynamics simulation assessment of inhibitors for thyroid hormone receptor α and β. *J. Mol. Model.* **2014**, *20*, 1−19.
(43) Wang, J.; Li, Y.; Yang, Y.; Du, J.; Zhang, S.; Yang, L. In silico research to assist the investigation of carboxamide derivatives as potent TRPV1 antagonists. *Mol. BioSyst.* **2015**, *11*, 2885−2899.
(44) Paeshuyse, J.; Leyssen, P.; Mabery, E.; Boddeker, N.; Vrancken, R.; Froeyen, M.; Ansari, I. H.; Dutartre, H.; Rozenski, J.; Gil, L. H. A novel, highly selective inhibitor of pestivirus replication that targets the viral RNA-dependent RNA polymerase. *J. Virol.* **2006**, *80*, 149−160.
(45) Salim, M. T.; Goto, Y.; Hamasaki, T.; Okamoto, M.; Aoyama, H.; Hashimoto, Y.; Musiu, S.; Paeshuyse, J.; Neyts, J.; Froeyen, M. Highly potent and selective inhibition of bovine viral diarrhea virus replication by γ-carboline derivatives. *Antiviral Res.* **2010**, *88*, 263−268.
(46) Paeshuyse, J.; Letellier, C.; Froeyen, M.; Dutartre, H.; Vrancken, R.; Canard, B.; De Clercq, E.; Gueiffier, A.; Teulade, J.-C.; Herdewijn, P. A pyrazolotriazolopyrimidinamine inhibitor of bovine viral diarrhea virus replication that targets the viral RNA-dependent RNA polymerase. *Antiviral Res.* **2009**, *82*, 141−147.
(47) Paeshuyse, J.; Chezal, J.-M.; Froeyen, M.; Leyssen, P.; Dutartre, H.; Vrancken, R.; Canard, B.; Letellier, C.; Li, T.; Mittendorfer, H. The imidazopyrrolopyridine analogue AG110 is a novel, highly selective inhibitor of pestiviruses that targets the viral RNA-dependent RNA polymerase at a hot spot for inhibition of viral replication. *J. Virol.* **2007**, *81*, 11046−11053.
(48) Castro, E. F.; Fabian, L. E.; Caputto, M. E.; Gagey, D.; Finkielsztein, L. M.; Moltrasio, G. Y.; Moglioni, A. G.; Campos, R. H.; Cavallaro, L. V. Inhibition of bovine viral diarrhea virus RNA synthesis by thiosemicarbazone derived from 5, 6-dimethoxy-1-indanone. *J. Virol.* **2011**, *85*, 5436−5445.
(49) Vrancken, R.; Paeshuyse, J.; Haegeman, A.; Puerstinger, G.; Froeyen, M.; Herdewijn, P.; Kerkhofs, P.; Neyts, J.; Koenen, F. Imidazo [4, 5-c] pyridines inhibit the in vitro replication of the classical swine fever virus and target the viral polymerase. *Antiviral Res.* **2008**, *77*, 114−119.

DOI: 10.1021/acs.jafc.6b01067
J. Agric. Food Chem. 2016, 64, 5941−5950